Microstructural theory and the rheology of concentrated colloidal suspensions

EHSSAN NAZOCKDAST[1] AND **JEFFREY F. MORRIS**[1]

[1]Benjamin Levich Institute and Department of Chemical Engineering, City University of New York, NY 10031, USA

(Received 15 September 2011)

A theory for the analytical prediction of microstructure of concentrated Brownian suspensions of spheres in simple-shear flow is developed. The computed microstructure is used in a prediction of the suspension rheology. A near-hard-sphere suspension is studied for solid volume fraction $\phi \leqslant 0.55$ and Péclet number $Pe = 3\pi\eta\dot{\gamma}a^3/k_bT \leqslant 100$; a is the particle radius, η is the suspending Newtonian fluid viscosity, $\dot{\gamma}$ is the shear rate, k_b is the Boltzmann constant and T is absolute temperature. The method developed determines the steady pair distribution function $g(\mathbf{r})$, where $\mathbf{r}$ is the pair separation vector, from a solution of the Smoluchowski equation (SE) reduced to pair level. To account for the influence of the surrounding bath of particles on the interaction of a pair, an integro-differential form of the pair SE is developed; the integral portion represents the forces due to the bath which drive the pair interaction. Hydrodynamic interactions are accounted in a pairwise fashion, based on the dominant influence of pair lubrication interactions for concentrated suspensions. The SE is modified to include the influence of shear-induced relative diffusion, and this is found to be a crucial for success of the theory; a simple model based on understanding of the shear-induced self-diffusivity is used for this property. The computation of the microstructure is split into two parts, one specific to near-equilibrium ($Pe \ll 1$), where a regular perturbation expansion of g in Pe is applied, and a general-

Pe solution of the full SE. The predicted microstructure at low Pe agrees with prior theory for dilute conditions, and becomes increasingly distorted from the equilibrium isotropic state as ϕ increases at fixed $Pe < 1$; Normal stress differences are predicted and the zero-shear viscosity predicted agrees with simulation results obtained using a Green-Kubo formulation (Foss, D. R. & Brady, J. F. 2000. *J. Fluid Mech.* **407**, 167–200). At $Pe \geqslant O(1)$, the influence of convection results in a progressively more anisotropic microstructure, with the contact values increasing with Pe to yield a boundary layer and a wake. Agreement of the predicted microstructure with observations from simulations is good. The predicted rheology captures shear thinning and shear thickening as well as normal stress differences in good agreement with simulation; quantitative agreement is best at large ϕ.

Key Words: Smoluchowski equation, nonequilibrium statistical physics, suspension rheology, suspension microstructure

---

1. Introduction

Colloidal suspensions can be found in a wide range of applications and natural flows including processing of cement and foodstuffs or flow of mud (Russel *et al.* 1995; Vermant & Solomon 2005). Colloidal suspensions, commonly also called dispersions, are complex fluids. These materials are distinct from simple fluids because the relative arrangement of the constituents, commonly referred to as microstructure, is determined by the interplay of particle scale forces with the motion imposed by macroscopic flow. A consequence of this coupling is that the properties become flow-rate dependent. Of these properties, we will be particularly interested in the rheology. Examples of complex fluids include

well-known non-Newtonian materials such as polymeric liquids and gels, in addition to colloidal suspensions.

We have a substantial theoretical understanding of the transport properties of simple liquids because these are determined primarily by equilibrium microstructure, for which experimental and theoretical understanding is well-developed (Hansen & MacDonald 1986). By contrast, the theoretical foundations for complex fluid rheology are incomplete, and the task is substantially more demanding than in the case of simple fluids. For complex fluids, the *nonequilibrium* microstructure must be determined for any condition (rate and composition), and then related through structure-property relations to the rheological properties.

This work describes a theoretical framework to determine the microstructure of hard-sphere colloidal suspensions, and demonstrates its application to prediction of the bulk rheological properties of the mixture. We consider the hard-sphere colloidal suspension, arguably the simplest complex fluid and thus a material for which a theory of some completeness is possible. The simplicity arises from the small number of parameters necessary to characterize the conditions. Because the size of the dispersed particles, a, is typically 10 nm to 1 μm, $Re_p = \rho\dot{\gamma}a^2/\eta \ll 1$, which implies that inertial effects at the particle scale can typically be neglected in colloidal dispersions, i.e. the dynamics may be assumed to take place at $Re_p = 0$; here we specify a as the particle radius, η is the fluid viscosity, and $\dot{\gamma}$ is the shear rate of the flow. Restricting attention to monodisperse spherical particles, the microstructure and properties of the hard-sphere dispersion in simple-shear flow can be expressed as functions of only two dimensionless parameters, one being the volume fraction of the solid phase, $\phi = 4\pi na^3/3$ where n is the particle number density, and the other the Péclet number, $Pe = \dfrac{3\pi\eta\dot{\gamma}a^3}{k_bT}$, which is the ratio of hydrodynamic (viscous) forces to Brownian forces. At $Pe = 0$, the dispersion is at

equilibrium, while $Pe \to \infty$ refers to the limit where the structure and rheology are governed by hydrodynamics. For computational ease, we find it necessary to include a short-ranged force and it is more appropriate to describe the system studied here as a 'nearly hard-sphere' dispersion. Despite their simplicity, nearly hard-sphere colloidal dispersions show rich non-Newtonian rheological behaviors including shear-thinning at low shear rates, shear thickening at high shear rates, and normal stress differences. These behaviors are seen in both experiments (van der Werff & de Kruiff 1989; Zarraga *et al.* 2000) and simulations (Foss & Brady 2000). The microstructure and resulting rheology of colloidal dispersions is of importance in describing such flow behaviors as shear-induced migration (Leighton & Acrivos 1987*b*; Morris & Boulay 1999) and abrupt shear thickening (Barnes 1989) and flow-induced jamming.

Simulation techniques such as Stokesian Dynamics (SD), which accurately capture the near-field lubrication interactions and far-field hydrodynamic interactions in sheared colloidal suspensions, allow investigation of the microstructure and rheology with valuable insight to the role of Brownian, hydrodynamic and interparticle forces on the dynamics of the dispersed phase and its impact on rheology (Brady & Bossis 1988; Sierou & Brady 2001). While the level of detail is not yet comparable to simulation, microscopy (Gao *et al.* 2010) and scattering studies (Chen *et al.* 1994) provide experimental measures of the relative distribution of particles. Theoretical study of the microstructure in sheared suspensions has made significant progress since the pioneering work of Batchelor & Green (1972*b*), but any theoretical formulation to date has been severely limited in its range of validity. The existing theories tend to explore either near-equilibrium conditions, i.e. $Pe \ll 1$, for which concentrated conditions have been studied (Fuchs & Cates 2002; Lionberger & Russel 1997; Brady 1993), or dilute conditions, $\phi \ll 1$ where $Pe \gg 1$ has been considered (Brady & Vicic 1995; Brady & Morris 1997; Bergenholtz *et al.* 2002).

This work utilizes certain elements of each of these groups of studies, in combination with essential novel features motivated by theory for the equilibrium liquid state, to provide a formulation describing the nonequilibrium response of colloidal dispersions over a wide range of ϕ and Pe.

Near equilibrium structure developed in weak shear flow remains predominately controlled by thermal forces and excluded volume. Therefore, theories in this limit are often based in liquid-state theory. In these works, the many-body thermodynamic coupling is modeled through the well-known integral equation formulations in liquid-state theory while the role of hydrodynamics has been either neglected (Szamel 2001) or approximated through simple mean-field arguments and near contact lubrication interactions (Lionberger & Russel 1997). Comparison with the available experimental data shows that the predictions are primarily controlled by the method used to account for thermodynamic coupling and different approximations of hydrodynamic functions have a minor influence. These results are limited to $Pe \ll 1$, and have not been extended to $Pe \geqslant 1$ where hydrodynamics becomes a controlling factor. The integral equation approaches, so successful for the equilibrium liquid state, are not readily extended to far-from-equilibrium conditions, but the concept of coupling direct and indirect interactions is utilized in our integro-differential formulation of the Smoluchowski equation (SE) for the pair structure. The essential feature which makes the pair SE appropriate for general flow conditions is that it represents a balance of the different and competing fluxes of pair probability, and thus flow is naturally captured. This is quite different from the relation of direct and indirect interactions appearing in such closures as the Percus-Yevick and hypernetted chain approximations (Hansen & McDonald 1986) for equilibrium structure.

The primary challenges in describing concentrated suspension microstructure at the pair level are to handle the many-body interaction, and to couple appropriately to the

'bath' representing the influence of the other particles under flow conditions. This intrinsically raises two basic issues, one being the need to relate the pair distribution function to the triplet distribution, say $g_3(\mathbf{r}, \mathbf{r}_{13})$, and higher particle-number distributions. The second is how to handle hydrodynamic interactions. We address both of these essential difficulties in the present work. The closure of the hierarchy involving g_3 is made using a modification of the Kirkwood superposition approximation, and more is detailed regarding the hydrodynamic interactions just below.

The problems associated with many-body hydrodynamics can be eliminated in dilute colloidal suspensions where interactions of more than two particles are assumed negligible. This allows one to use isolated pair hydrodynamic functions, and shear-induced diffusion is negligible. These dilute theories provide an understanding of the nature of anisotropic pair structure and the consequent nonlinear rheology observed at $Pe \gg 1$. Brady & Morris (1997) showed analytically that at $Pe \gg 1$, there is a singular influence of short-ranged interparticle forces, as these break the pair microstructural symmetry associated with Stokes flow, leading to normal stress differences which do not vanish as $Pe \to \infty$. The pair structure becomes highly anisotropic, and develops boundary layer in $g(\mathbf{r})$ near contact where convection balances diffusion. Bergenholtz *et al.* (2002) solved the dilute pair SE for simple-shear flow numerically over a wide range of Pe, and showed the development of the wake corresponding to the noted boundary layer. They were able to predict shear thinning at low Pe and shear thickening at large Pe, as well as a change in sign of the first normal stress difference with increase of Pe, as also seen in simulations at elevated ϕ. Thus certain behavior in more concentrated suspensions is captured by dilute theories, but much is not properly captured. Attempts to extend the dilute theories to higher ϕ through scaling analysis (Brady & Morris 1997; Foss & Brady 2000) assume that the effective mean-field outside the boundary layer can be represented by a uniform

fluid with modified viscosity scaling as high frequency viscosity, $\eta_\infty(\phi)$ at the desired ϕ. However, detailed study of $g(\mathbf{r})$ from SD simulations at $Pe = 1 - 1000$ by Morris & Katyal (2002) shows that the microstructural anisotropy changes qualitatively as ϕ increases at fixed Pe. Specifically, at large Pe, the maximum value of $g(\mathbf{r})$ shifts from being near the compressional axis for $\phi \leqslant 0.3$ to along the flow direction for $\phi \geqslant 0.35$; this is reflected in rheology significantly differing from what one would predict using the scaling arguments. These rheological changes are most pronounced in the highly structurally dependent normal stress differences. This shows the need for a detailed treatment of the structure at large ϕ in sheared dispersions.

The present formulation provides a self-consistent method for modeling many-body hydrodynamic interactions in concentrated suspensions at $Pe \gg 1$ and the resulting rheology. The theory is motivated by the observation that particles near contact control the properties and dynamics in concentrated sheared suspensions. This point was used by Lionberger & Russel (1997), who proposed different approximations of hydrodynamic functions based on mean-field arguments and near contact lubrication interactions. The present theory of the microstructure is built on the assumption that short-range lubrication interactions determine the dynamics of particles, and on the recognition that shear-induced diffusion plays an important role in setting the microstructure. The formulation developed here can, in principle, be applied over the entire range of Pe and ϕ, although here we limit the investigation to $Pe \leqslant 100$ and $0.1 \leqslant \phi \leqslant 0.55$. The resolution of current experimental techniques is not high enough to probe the details of microstructure, and as an alternative we compare predictions of the theory with results of our own Accelerated Stokesian Dynamics (Banchio & Brady 2003; Sierou & Brady 2001) simulations.

The paper begins in §2 with the formulation of the problem, and elaborates the steps

taken to arrive at a closed integro-differential Smoluchowski equation for the pair distribution function, $g(\mathbf{r})$. This is followed, in §3, by the description of the particle stress contributions in terms of the pair microstructure. The solution technique for the microstructure equation is presented in §4. Predictions of microstructure and rheology at various Pe and ϕ, and their comparison with simulations, are given in §5.1 and §5.2, respectively.

2. Microstructure

2.1. *Smoluchowski equation of motion*

We consider suspensions at very small particle-scale Reynolds number, so that inertia is negligible and the motion can be described by Stokes equations. The microstructure is assumed to be governed by the Smoluchowski equation, which for the N-particle configuration space is written

$$\frac{\partial P_N}{\partial t} + \sum_{\alpha=1}^{N} \nabla_\alpha \cdot (\mathbf{j}_\alpha) = 0, \tag{2.1}$$

where $P_N(\mathbf{x}_1, \mathbf{x}_2, ..., \mathbf{x}_N)$ is the N-particle configurational probability distribution, and $\mathbf{j}_\alpha$ is the probability flux associated with particle α. The flux is expressed as

$$\mathbf{j}_\alpha = \left(\mathbf{U}_\alpha + \sum_{\beta=1}^{\beta=N} \mathbf{M}^{FU}_{\alpha\beta} \cdot \mathbf{F}_\beta \right) P_N - \sum_{\beta=1}^{\beta=N} \mathbf{D}_{\alpha\beta} \cdot \nabla_\beta P_N, \tag{2.2}$$

where $\mathbf{U}_\alpha$ is the velocity of particle α induced by bulk flow and hydrodynamic interactions with other particles, $\mathbf{M}_{\alpha\beta}$ is the mobility of particle α to a force on particle β, and $\mathbf{D}_{\alpha\beta} = kT$ is the diffusion tensor. The force exerted on particle β may be expressed in terms of an interparticle potential energy as $\mathbf{F}_\beta = -\nabla_\beta V$.

To reduce to an equation for the pair microstructure, (2.1) is integrated over all possible

configurations of $N-2$ particles keeping two particles fixed, which yields

$$\nabla_1 \cdot \langle\, \mathbf{j}_1 \,\rangle_2 + \nabla_2 \cdot \langle\, \mathbf{j}_2 \,\rangle_2 = 0, \tag{2.3}$$

where $\langle \quad \rangle_2$ is defined by

$$P_2 \langle\, A \,\rangle_2(\mathbf{x}_1, \mathbf{x}_2) = N(N-1) \int A P_N d\mathbf{x}_3 d\mathbf{x}_4 ... d\mathbf{x}_N. \tag{2.4}$$

When gradients and fluxes are expressed in terms of the relative position vector, $\mathbf{r} = \mathbf{x}_2 - \mathbf{x}_1$, (2.3) simplifies to

$$\nabla_{\mathbf{r}} \cdot \langle \mathbf{j}_2 - \mathbf{j}_1 \,\rangle_2 = 0. \tag{2.5}$$

Applying (2.2) to (2.5) yields:

$$\nabla_{\mathbf{r}} \cdot \Bigg(\langle\, \mathbf{U} \,\rangle_2 P_2 + \langle \mathbf{M} \cdot \mathbf{F} \rangle_2 P_2 - \langle \mathbf{D} \rangle_2 \cdot \nabla_{\mathbf{r}} P_2 + n \int \Big(\big\langle \big(\mathbf{M}_{23} - \mathbf{M}_{13} \big) \cdot \mathbf{F}_3 \big\rangle_3 P_3 - \langle \mathbf{D}_{23} - \mathbf{D}_{13} \rangle_3 \cdot \nabla_3 P_3 \Big) d\mathbf{x}_3 \Bigg) = 0, \tag{2.6}$$

with

$$\mathbf{U} = \mathbf{U}_2 - \mathbf{U}_1, \tag{2.7a}$$

$$\mathbf{D} = 2\big(\mathbf{D}_{11} - \mathbf{D}_{12} \big), \tag{2.7b}$$

$$\mathbf{M} = 2\big(\mathbf{M}_{11}^{FU} - \mathbf{M}_{12}^{FU} \big) = 2\big(\mathbf{R}_{11}^{FU} - \mathbf{R}_{12}^{FU} \big)^{-1}, \tag{2.7c}$$

and

$$\mathbf{F} = \frac{\mathbf{F}_2 - \mathbf{F}_1}{2}. \tag{2.7d}$$

Here, $\mathbf{R}^{FU}$ is the resistance tensor coupling velocity to force, with the subscript 12 indicating this is the coupling of the force on particle 1 due to motion of particle 2. The integral term on the right hand side (RHS) of (2.6) is the additional flux induced by the forces on the other $N-2$ particles. The probability of finding a third particle between $\mathbf{x}_3$ and $\mathbf{x}_3 + d\mathbf{x}_3$ when particles 1 and 2 lie between $\mathbf{x}_1$ and $\mathbf{x}_1 + d\mathbf{x}_1$ and $\mathbf{x}_2$ and $\mathbf{x}_2 + d\mathbf{x}_2$,

respectively, is given by $P_3 d\mathbf{x}_3$. The mean relative velocity $\langle \mathbf{U} \rangle_2$ is obtained by averaging the relative velocity of the pair at each $\mathbf{r}$, over all configurations of the remaining $N-2$ particles.

The relative velocity in each configuration fluctuates around the average value and the velocity fluctuations result in a diffusion process. In a quiescent state, associated with an equilibrium structure, Brownian velocity fluctuations drive the diffusion represented by the well-known Stokes-Einstein relationship: $\mathbf{D}_{\alpha\beta} = k_b T \mathbf{M}^{FU}_{\alpha\beta}$. Shear flow also drives a random walk which may be described as a diffusion; this phenomenon is known as shear-induced diffusion (Leighton & Acrivos 1987*a*; Sierou & Brady 2004). While Brownian diffusion is proportional to the thermal energy of the system, $k_b T$, shear-induced diffusion scales with the shear rate, and is thus the dominant diffusion mechanism at elevated shear rates, i.e. at large Pe. To formulate a predictive theory for the microstructure and rheology of a concentrated dispersion at $Pe > 1$, it is found to be essential to include the shear-induced diffusion, as we will illustrate in the results section. However, as seen in (2.6), systematic integration of the Smoluchowski equation does not take into account shear induced velocity fluctuations and the resulting *shear-induced relative diffusion* between a pair of particles. We note that there is no prior published work which has addressed the shear-induced relative diffusion, which we incorporate as

$$\langle \mathbf{D} \rangle_2 = k_b T \langle \mathbf{M} \rangle_2 + \langle \mathbf{D}^{\dot{\gamma}} \rangle_2, \tag{2.8}$$

where $k_b T \langle \mathbf{M} \rangle_2$ is the Brownian diffusion and $\langle \mathbf{D}^{\dot{\gamma}} \rangle_2$ is the shear-induced diffusion, whose functionality will be discussed below.

The combined force and torque balance for non-Brownian particles interacting only through hydrodynamics can be formulated as

$$\mathbf{R}^{FE} : \mathbf{E}^{\infty} - \mathbf{R}^{FU} \cdot (\mathbf{U} - \mathbf{U}^{\infty}) = 0, \tag{2.9}$$

where the resistance functions, $\mathbf{R}^{FE}$ (coupling force and torque to a bulk straining motion) and $\mathbf{R}^{FU}$ (coupling force and torque to velocity), are functions of the N-particle configuration. For an isolated pair, the resistance tensors are well-known (Kim & Karrila 2005), and are only a function of pair separation vector, $\mathbf{r}$. Following (2.9), the relative pair velocity can be written

$$\mathbf{U}_\alpha = \mathbf{U}_\alpha^\infty + (\mathbf{R}^{FU})^{-1} \cdot \left(\mathbf{R}^{FE} : \mathbf{E}^\infty\right)_\alpha , \tag{2.10}$$

where α labels the particle of interest. By contrast, with no hydrodynamic interactions, the relative translational/angular pair velocity in a suspension with an external flow and interparticle forces is

$$\mathbf{U}_\alpha = \mathbf{U}_\alpha^\infty + (\mathbf{R}^{FU})^{-1} \cdot \mathbf{F}_\alpha, \tag{2.11}$$

where $\mathbf{R}^{FU} = 6\pi\eta a\mathbf{I}$ is simply a Stokes drag coefficient for this case.

Comparing (2.10) and (2.11) reveals a similarity. The force, $\mathbf{F}_\alpha$, is replaced by $(\mathbf{R}^{FE} : \mathbf{E}^\infty)_\alpha$ in (2.10). Hydrodynamic interactions may thus be thought of as a composition of two generally opposing forces: (1) the external force that drives the suspension flow and gives rise to velocity $\mathbf{U}_\alpha^\infty$, and (2) the resisting force that imposes the effect of excluded volume through fluid/particle interaction, $\mathbf{R}^{FE} : \mathbf{E}^\infty$. When no other forces are present, these forces must be equal and opposite to yield a force-free (and torque-free) motion. We call the second of these forces the *lubrication force*, $\mathbf{F}^{lub} = \mathbf{R}^{FE} : \mathbf{E}^\infty$, to indicate the predominate role of lubrication interactions for the conditions we will study. Including the known pair resistance functions, the lubrication force that particle 2 applies on particle 1 for an isolated pair is

$$\mathbf{F}_{21}^{lub} = -6\pi\eta a\Big(X(r)(\hat{\mathbf{r}} \cdot \mathbf{E} \cdot \hat{\mathbf{r}})\hat{\mathbf{r}} + Y(r)\big(\mathbf{E} \cdot \hat{\mathbf{r}} - (\hat{\mathbf{r}} \cdot \mathbf{E} \cdot \hat{\mathbf{r}})\hat{\mathbf{r}}\big)\Big). \tag{2.12}$$

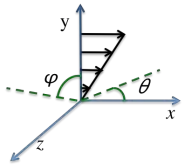

FIGURE 1. A schematic of the angle definitions and flow direction. θ is the azimuthal angle measured clockwise from the positive x axis and φ is the polar angle measured from $x-y$ plane.

Limiting values of the radially-dependent functions are

$$X(r) = \epsilon^{-1} \quad r \to 2; \quad X(r) = \frac{5}{r^2} \quad r \gg 1$$

,

$$Y(r) = 0.271 \ln(\epsilon^{-1}) \quad r \to 2; \quad Y(r) = \frac{16}{3r^4} \quad r \gg 1,$$

where $r = |\mathbf{r}|/a$, $\hat{\mathbf{r}} = \mathbf{r}/r$ and $\epsilon = r/a - 2$. The first term on the RHS of (2.12) is the lubrication force along the line of centers, and the second term is the force in the plane normal to the line of centers, i.e. the local $\hat{\theta} - \hat{\varphi}$ plane. The definitions of angles and directions are shown in figure 2.1.

Recall that the lubrication force is repulsive in case of particles approaching, and is attractive while they are being separated. Integrating (2.10) to the pair level yields

$$\langle \mathbf{U} \rangle_2 = \mathbf{U}^\infty + \langle \mathbf{M} \cdot \mathbf{F}^{\text{lub}} \rangle_2 . \tag{2.13}$$

We now make a mean-field approximation by assuming that the pair is immersed in a field that contains the average effect of the bath of the other particles. As a consequence of this approximation, we neglect the convection flux induced by fluctuations in force and mobility; however these fluctuations give rise to a diffusive flux which is captured through shear-induced relative diffusion, $\langle \mathbf{D}^{\dot{\gamma}} \rangle_2$ in 2.8. The conditional averages are therefore simplified as:

$$\langle \mathbf{M} \cdot \mathbf{F} \rangle_2 = \langle \mathbf{M} \rangle_2 \cdot \langle \mathbf{F} \rangle_2 . \tag{2.14}$$

The mean-field approximation is expected to be valid if the suspension is not near maximum packing. Mean-field assumption allows the integral term in (2.6) to be modified as follows:

$$\int \left(\left\langle \left(\mathbf{D}_{23} - \mathbf{D}_{13} \right) \cdot \mathbf{F}_3 \right\rangle_3 P_3 - \left\langle \mathbf{D}_{23} - \mathbf{D}_{13} \right\rangle_3 \cdot \nabla_3 P_3 \right) d\mathbf{x}_3 \approx \left(\int \left\langle \mathbf{D}_{23} - \mathbf{D}_{13} \right\rangle_3 P_3 d\mathbf{x}_3 \right) \left(\int \left\langle \mathbf{F}_3 - \nabla_3 \ln(P_3) \right\rangle_3 P_3 d\mathbf{x}_3 \right) = 0, \tag{2.15}$$

as both terms on the RHS are identically zero, bases on pair-particle symmetries. After including lubrication forces, and applying the mean-field assumption, (2.6) is modified to

$$\nabla_{\mathbf{r}} \cdot \left(\mathbf{U}^{\infty} g + \langle \mathbf{M} \rangle_2 \cdot \left(\langle \mathbf{F}^{HS} \rangle_2 + \langle \mathbf{F}^{lub} \rangle_2 \right) g - \langle \mathbf{D} \rangle_2 \cdot \nabla_{\mathbf{r}} g \right) = 0, \tag{2.16}$$

where $\mathbf{F}^{HS}$ represents forces due to potential interaction, and $g = P_2/N$ is the pair distribution function. Quantities are made dimensionless by scaling as follows:

$$\begin{gathered} \mathbf{r} \sim a; \quad \mathbf{D} \sim D_0; \quad \mathbf{M} \sim D_0/k_b T. \\ \mathbf{F}^{HS} \sim k_b T/a; \quad \mathbf{F}^{lub} \sim 3\pi\eta\dot{\gamma}a^2; \quad \mathbf{U}^{\infty} \sim \dot{\gamma}a, \end{gathered} \tag{2.17}$$

where $D_0 = k_b T/6\pi\eta a$. In dimensionless form, (2.16) becomes

$$\nabla \cdot \left(\mathbf{U}^{\infty} g + \langle \mathbf{M} \rangle_2 \cdot \left(Pe \langle \mathbf{F}^{lub} \rangle_2 + \langle \mathbf{F}^{HS} \rangle_2 \right) g - Pe^{-1} \langle \mathbf{D} \rangle_2 \cdot \nabla g \right) = 0, \tag{2.18}$$

where ∇ is the dimensionless $\nabla_{\mathbf{r}}$, and we have defined the Péclet number,

$$Pe = \frac{\dot{\gamma}a^2}{2D_0} = \frac{3\pi\eta\dot{\gamma}a^3}{k_b T}. \tag{2.19}$$

The boundary conditions are

$$\mathbf{j}_{\mathbf{r}} = 0 \quad \text{at} \quad r = 2, \tag{2.20a}$$

$$g \sim 1 \quad \text{as} \quad r \to \infty. \tag{2.20b}$$

The first boundary condition implies zero radial flux at contact.

2.2. *Conditional Averages*

In the convection-diffusion equation for the pair microstructure, the conditionally-averaged quantities $\langle \mathbf{F}^{lub} \rangle_2$, $\langle \mathbf{F}^{HS} \rangle_2$, $\langle \mathbf{M} \rangle_2$ and $\langle \mathbf{D} \rangle_2$ should be self-consistently expressed in terms of $\mathbf{r}$ and g. To determine the conditional averages present in (2.18) in principle requires including many-body hydrodynamic interactions. This is intractable, and we make approximations based on the observation from experiments and simulation results that the controlling configuration in concentrated sheared colloidal suspensions is particles near contact, where lubrication interactions control the dynamics. These interactions can then be assumed to be summations of individual pair lubrication interactions; we assume that long-range many-body hydrodynamic interactions have little effect on the structure and are negligible. By treating the hydrodynamic interactions in this pair-wise additive fashion, the problem is tractable, and the results described later support the validity of the approximation for concentrated suspensions.

2.2.1. *Mean forces,* $\langle \mathbf{F}^{HS} \rangle_2$ *and* $\langle \mathbf{F}^{lub} \rangle_2$*:*

We begin by considering $\mathbf{F}^{HS}$ and $\mathbf{F}^{lub}$, both of which are steeply decaying functions of r near contact. Due to the symmetry of the pair geometry, $\langle \mathbf{F}_1 \rangle_2 = -\langle \mathbf{F}_2 \rangle_2$. Applying the assumption of pair-wise additivity, the average force on particle 1, $\langle \mathbf{F}_1 \rangle_2$ is formulated as

$$\langle \mathbf{F}_1 \rangle_2 g(\mathbf{r}) = \mathbf{F}_{21}(\mathbf{r}) g(\mathbf{r}) + n \int \mathbf{F}_{31}(\mathbf{r}_{31})\, g_3(\mathbf{r}, \mathbf{r}_{31}) d\mathbf{r}_{31}, \tag{2.21}$$

where $\mathbf{F}_{21}$ and $\mathbf{F}_{31}$ are forces individual particles 2 and 3 exerted on particle 1 respectively, and $\mathbf{r}_{31} = \mathbf{x}_3 - \mathbf{x}_1$. A steep repulsion was used to model hard-sphere forces:

$$\mathbf{F}_{21}^{HS} = -F_0 \frac{\tau e^{-\tau\epsilon}}{1 - e^{-\tau\epsilon}} \hat{\mathbf{r}}; \quad F_0 = k_b T/a, \tag{2.22}$$

where we recall that $\epsilon = r - 2$. The parameter τ controls the steepness of the repulsive force, and we have used $\tau = 200$ for all calculations reported here. The hydrodynamic force, $\mathbf{F}^{lub}$, is defined according to (2.12).

It is necessary to express the triplet distribution, g_3, in terms of pair distribution function, g, through a closure approximation. A superposition approximation proposed by Rice & Lekner (1965), given by

$$g_3(\mathbf{x}_1, \mathbf{x}_2, \mathbf{x}_3) = g(\mathbf{r}_{21}) g(\mathbf{r}_{31}) g(\mathbf{r}_{32}) \exp\left[\tau^\star(\mathbf{r}, \mathbf{r}_{31}, \phi)\right], \tag{2.23}$$

was used in this work. This closure modifies the standard Kirkwood superposition approximation through the final exponential term which models interactions of particles 1, 2 and 3 with other particles through numerical evaluation of "irreducible cluster integrals"; Rice & Lekner (1965) extended this cluster expansion to 5 particles level using a Padé expansion. We do not reproduce the full details here, but the interested reader may find these in Table 1 and equations 13 and 14 in the Rice & Lekner paper. This approximation gives very good agreement at equilibrium, $Pe = 0$, up to $\phi = 0.40$, the upper limit on ϕ for the Kirkwood approximation for the equilibrium triplet structure in hard-sphere liquids. Yurkovetsky & Morris (2006) showed in their study of triplet correlation that the standard Kirkwood approximation gives a reasonable measure of triplet distribution at $Pe \gg 1$. The modified Kirkwood approximation is simple in format and gives reasonable accuracy at $Pe \gg 1$; there is no obvious candidate to replace this closure for nonequilibrium conditions. Applying (2.23) in (2.21) gives

$$\langle \mathbf{F}_1 \rangle_2 = \mathbf{F}_{21}(\mathbf{r}) + n \int \mathbf{F}_{31}(\mathbf{r}_{31})\, g(\mathbf{r}_{32}) g(\mathbf{r}_{31}) \exp\left[\tau^\star(\mathbf{r}_{31}, \mathbf{r}, \phi)\right] d\mathbf{r}_{31}. \tag{2.24}$$

2.2.2. *Mean relative mobility,* $\langle \mathbf{M} \rangle_2$*:*

To evaluate the mean relative mobility, we first calculate $\langle \mathbf{R} \rangle_2$, and then use $\langle \mathbf{M} \rangle_2 = \langle \mathbf{R} \rangle_2^{-1}$. The first level of approximation for formulating many-body effects is to consider the effect of a third particle on $\langle \mathbf{R} \rangle_2$. We write

$$\langle \mathbf{R} \rangle_2(\mathbf{r}) g = \mathbf{R}_{pair}(\mathbf{r}) g + n \int \Big(\mathbf{R}(\mathbf{r}, \mathbf{r}_{31}, \mathbf{r}_{32}) - \mathbf{R}_{pair}(\mathbf{r}) \Big) \, g_3 d\mathbf{r}_{31}, \tag{2.25}$$

where $\mathbf{R}(\mathbf{r}, \mathbf{r}_{31}, \mathbf{r}_{32})$ is the resistance for particles 1 and 2 in the presence of a third particle and $\mathbf{R}_{pair}(\mathbf{r})$ is the resistance of the isolated pair 1 and 2; note that these are the resistances associated with relative motion of the pair. The term in parenthesis in the integrand of (2.25) is therefore the increase of the resistance to pair relative motion with respect to the isolated pair due to the other particles captured through the third-particle integral. To calculate the resistance components in triplet configurations for particles near contact, the resistance is assumed to be pair-wise additive; for well-separated particles, the third-particle effect on mobility is modeled through the method of reflections (Mazoor & Van Saarloos 1982), and the mobility is inverted to obtain the modified resistance. For intermediate separations $\mathbf{R}(\mathbf{r}, \mathbf{r}_{31}, \mathbf{r}_{32})$ is obtained by interpolating between the near contact and far-field results. This formulation imposes the effect of excluded volume in a probabilistic fashion. For example, consider three closely-spaced particles along one line with particle 3 between particles 1 and 2. In this case, particle 3 strongly inhibits movement of particles 1 and 2 along their line of centers, and causes a significant increase in resistance in this direction. If the third particle is far from both particles 1 and 2, it has a small effect on the relative resistance.

After evaluating $\mathbf{R}(\mathbf{r}, \mathbf{r}_{31}, \mathbf{r}_{32})$ and applying (2.23), the average resistance, $\langle \mathbf{R} \rangle_2$, is now only a function of g and $\mathbf{r}$. It is inverted to obtain $\langle \mathbf{M} \rangle_2 = \langle \mathbf{R} \rangle_2^{-1}$.

2.2.3. *Mean relative diffusivity,* $\langle \mathbf{D} \rangle_2$*:*

As noted previously, Brownian diffusion and shear-induced diffusion are captured in a single relative diffusivity. Note that after scaling using 2.17, the Brownian diffusion is, in dimensionless form, equal to the mobility, $\langle \mathbf{M} \rangle_2$ formulated above. The shear-induced relative diffusion is the result of velocity fluctuations directly related to the microstructure (Morris & Brady 1996; Brady & Morris 1997), which makes formulation of shear-induced diffusion a difficult task even at the single particle level. While the relative diffusivity due to shearing has not been well-studied, an approximation is obtained by considering particles near contact and widely separated. When $r \gg 1$, the motions of the two particles become uncorrelated, and shear-induced diffusion is the summation of individual shear induced self-diffusion coefficients of each particle, i.e. $2\mathbf{D}_s^{\dot{\gamma}}$, a quantity which has been well-studied and thus is assumed known from simulations or experiments for each concentration (Foss & Brady 2000). Near contact, $r-2 \to 0$, the relative velocity along the line of centers goes to zero, and thus both radial velocity fluctuations and the radial relative diffusivity vanish. The pair may, however, rotate around the center of mass, and thus velocity fluctuations remain in the angular (θ and φ) directions. These considerations lead to a simple form for $\left\langle \mathbf{D}^{\dot{\gamma}} \right\rangle_2$, given in dimensionless form by

$$\left\langle \mathbf{D}^{\dot{\gamma}} \right\rangle_2 = \frac{D^*}{D_0}\Big(\mathcal{A}(r)\hat{\mathbf{r}}\hat{\mathbf{r}} + \mathcal{B}(r)(\mathbf{I} - \hat{\mathbf{r}}\hat{\mathbf{r}})\Big), \tag{2.26}$$

where D^* is the far-field isotropic shear-induced self diffusivity. Simulation and experimental results show that shear-induced self diffusion is mildly anisotropic and slightly stronger in flow direction. We neglect this anisotropy and approximate the far-field relative diffusion with the strongest shear induced self-diffusion component, $D^* = D_s^{xx}$, which is known from prior work (Foss & Brady 2000). The function $\mathcal{A}(r)$ determines the radial variation of the diffusion coefficient in the r direction, while $\mathcal{B}(r)$ determines this

radial variation for the θ and φ directions. While relative motion of a pair of particles along the line of centers may be highly restricted by other particles, relative motion in the angular directions is less influenced. Lacking a clearly better choice, we assume that the shear-induced diffusion takes on the far field value at all separations for directions other than r, and thus $\mathcal{B}(r) = 1$. The function $\mathcal{A}(r)$ is approximated as

$$\mathcal{A}(r) = \begin{cases} 1 & r \geqslant 4. \\ e^{-n\left(\frac{4-r}{r-2}\right)} & r < 4, \end{cases} \tag{2.27}$$

so that it decays from unity at $r = 4$ to 0 at $r = 2$. For larger values of n, the decay is more rapid, but we note that for any n, $\mathcal{A}(r) \ll r - 2$ as $r \to 2$ so that relative radial diffusion is dominated by the Brownian contribution sufficiently close to contact.

The value of n is a controlling parameter for the microstructure, and it is effectively the only adjustable parameter in the theory. For each ϕ at $Pe > 1$, there is a critical n value beyond which a convergent solution cannot be obtained. This limiting largest value of n was determined for each ϕ and Pe studied, and results are reported only for this value. Physically, this retains just enough shear-induced diffusion near contact to maintain a stable disordered state.

This completes the formulation of a closed problem for the microstructure. All averaged values in (2.18) are expressed in terms of g and $\mathbf{r}$, and g will be determined by solving the integro-differential equation (2.18) with boundary conditions expressed by (2.20a) and (2.20b).

The formulation in this form is, however, not convenient for obtaining structural changes of $O(Pe^2)$ near equilibrium ($Pe \ll 1$). To address this weak perturbation limit, we expand $g(\mathbf{r})$ in terms of Pe, similar to regular perturbation techniques used previously for dilute suspensions (Batchelor 1977; Brady & Vicic 1995):

$$g\left(\mathbf{r}\right) = g^{eq}\left(r\right) + Pe\, g^{(1)}\left(\mathbf{r}\right) + Pe^2\, g^{(2)}\left(\mathbf{r}\right) + O(Pe^{5/2}), \tag{2.28}$$

where the superscript eq implies the equilibrium structure. The rheology is Newtonian to $O(Pe)$ and for obtaining non-Newtonian rheology the expansion should be pursued to Pe^2 (Brady & Vicic 1995). Incorporating the expansion to (2.16), equations are obtained for g^{eq}, $g^{(1)}$ and $g^{(2)}$. The equation governing $g^{eq}(r)$ is

$$\nabla \cdot \left(\left\langle \mathbf{U}^{eq} \right\rangle_2 (r)\, g^{eq}(r) + \left\langle \mathbf{M}^{eq} \right\rangle_2 (r) \cdot \nabla g^{eq}(r) \right) = 0, \tag{2.29}$$

where $\mathbf{U}^{eq}$ is defined by

$$\left\langle \mathbf{U}^{eq} \right\rangle_2 (r) = \left\langle \mathbf{M}^{eq} \right\rangle_2 (r) \cdot \left(\mathbf{F}^{HS}(\mathbf{r}) + n \int \mathbf{F}^{HS}(\mathbf{r}_{31})\, g^{eq}(r_{31})\, g^{eq}(r_{32}) \exp(\tau^\star)\, \mathbf{dr}_{31} \right). \tag{2.30}$$

The quantities are rendered dimensionless using the scalings given by (2.17). For $Pe \ll 1$, shear-induced diffusion can be neglected in comparison with Brownian diffusion, and therefore we have $\left\langle \mathbf{M}^{eq} \right\rangle_2 (r) = \left\langle \mathbf{D}^{eq} \right\rangle_2 (r)$ in the dimensionless form. Due to the noted limitation of the Kirkwood superposition closure at high concentrations, $g^{eq}(r)$ was obtained using the Percus-Yevick approach (Throop & Bearman 1965).

The equation governing $g^{(1)}(\mathbf{r})$ is

$$\nabla \cdot \left(\left\langle \mathbf{U}^{1} \right\rangle_2 g^{eq}(r) + \left\langle \mathbf{U}^{eq} \right\rangle_2 (r)\, g^{(1)}(\mathbf{r}) + \left\langle \mathbf{M}^{eq} \right\rangle_2 (r) \cdot \nabla g^{(1)}(\mathbf{r}) \right) = 0, \tag{2.31}$$

where $\left\langle \mathbf{U}^{eq} \right\rangle_2 (r) = \left\langle \mathbf{M}^{eq} \right\rangle_2 (r) \cdot \nabla \ln\left(g^{eq}(r)\right)$, from (2.29). The velocity $\left\langle \mathbf{U}^{1} \right\rangle_2$ is given by

$$\begin{aligned} \left\langle \mathbf{U}^{1} \right\rangle_2 (\mathbf{r}) = \left\langle \mathbf{M}^{eq} \right\rangle_2 (r) \cdot \Bigg(& \mathbf{F}^{lub}(\mathbf{r}) + n \int \mathbf{F}^{lub}(\mathbf{r}_{31})\, g^{eq}(\mathbf{r}_{31})\, g^{eq}(\mathbf{r}_{32}) \exp(\tau^\star)\, d\mathbf{r}_{31} \\ & + n \int \mathbf{F}^{HS}(\mathbf{r}_{31}) \left(g^{(1)}(\mathbf{r}_{31})\, g^{eq}(\mathbf{r}_{32}) + g^{1}(\mathbf{r}_{32})\, g^{eq}(\mathbf{r}_{31}) \right) \exp(\tau^\star)\, d\mathbf{r}_{31} \Bigg). \end{aligned} \tag{2.32}$$

The boundary conditions are zero radial flux at the contact surface ($r = 2$) and $g^{(1)} \to 0$ as $r \to \infty$. Substituting (2.32) in (2.31) yields an equation with only $g^{(1)}$ unknown.

The equation governing $g^2(\mathbf{r})$ is

$$\nabla \cdot \Big(\left\langle \mathbf{U}^2 \right\rangle_2 g^{eq}(r) + \left\langle \mathbf{U}^1 \right\rangle_2 (\mathbf{r})\, g^{(1)}(\mathbf{r}) + \langle \mathbf{U}^{eq} \rangle_2 (r)\, g^{(2)}(\mathbf{r}) + \langle \mathbf{M}^{eq} \rangle_2 (r) \cdot \nabla g^{(2)}(\mathbf{r}) \Big) = 0, \tag{2.33}$$

where $\left\langle \mathbf{U}^1 \right\rangle_2 (\mathbf{r})\, g^{(1)}(\mathbf{r})$ is known from the previous step and $\left\langle \mathbf{U}^2 \right\rangle_2$ is given by

$$\begin{aligned} \left\langle \mathbf{U}^2 \right\rangle_2 (\mathbf{r}) = \langle \mathbf{M}^{eq} \rangle_2 (r) \cdot \Bigg(& n \int \mathbf{F}^{HS}(\mathbf{r}_{31})\, g^{(1)}(\mathbf{r}_{31})\, g^{(1)}(\mathbf{r}_{32}) \exp(\tau^\star)\, d\mathbf{r}_{31} \\ & + n \int \mathbf{F}^{lub}(\mathbf{r}_{31}) \Big(g^{(1)}(\mathbf{r}_{31})\, g^{eq}(\mathbf{r}_{32}) + g^{eq}(\mathbf{r}_{31}) g^{(1)}(\mathbf{r}_{32}) \Big) \exp(\tau^\star)\, d\mathbf{r}_{31} \\ & + n \int \mathbf{F}^{HS}(\mathbf{r}_{31}) \Big(g^{(2)}(\mathbf{r}_{31})\, g^{eq}(\mathbf{r}_{32}) + g^{(2)}(\mathbf{r}_{32})\, g^{eq}(\mathbf{r}_{31}) \Big) \exp(\tau^\star)\, d\mathbf{r}_{31} \Bigg). \end{aligned} \tag{2.34}$$

The boundary conditions are again no flux at contact and $g^{(2)} \to 0$ as $r \to \infty$. Substituting (2.34) in (2.33) and using $g^{(1)}(\mathbf{r})$ determined in the previous step, the only unknown is $g^{(2)}(\mathbf{r})$. The solution technique used for solving these integro-differential equations is similar to the method used for general Pe, to be described in §4.

3. Rheology

We start with the formal expressions for suspension stress. The bulk stress in the suspension is given by

$$\langle \boldsymbol{\Sigma} \rangle = P\mathbf{I} + 2\eta \mathbf{E}^\infty + n \left(\langle \mathbf{S}^P \rangle + \langle \mathbf{S}^H \rangle + \langle \mathbf{S}^B \rangle \right), \tag{3.1}$$

where $P\mathbf{I} + 2\eta\mathbf{E}^\infty$ is the pure fluid stress contribution, and the other terms are stresses contributed by the particle phase. The contributions by individual particles are the stresslets $\langle \mathbf{S}^B \rangle$, $\langle \mathbf{S}^H \rangle$ and $\langle \mathbf{S}^P \rangle$, giving the Brownian, hydrodynamic, and interparticle stress contributions, respectively. Here, $\langle\ \rangle$ denotes an ensemble average taken over all particles and configurations. These stress contributions can be expressed in terms of

resistance tensors as (Brady 1993; Brady & Morris 1997)

$$\left\langle \mathbf{S}^{B} \right\rangle = -k_b T \left\langle \nabla \cdot \left(\mathbf{R}^{SU} \cdot (\mathbf{R}^{FU})^{-1} \right) \right\rangle, \tag{3.2a}$$

$$\left\langle \mathbf{S}^{H} \right\rangle = \left\langle \mathbf{R}^{SU} \cdot (\mathbf{R}^{FU})^{-1} \cdot \mathbf{R}^{FE} - \mathbf{R}^{SE} \right\rangle : \mathbf{E}^{\infty}, \tag{3.2b}$$

$$\left\langle \mathbf{S}^{P} \right\rangle = -\left\langle \left(\mathbf{x}\mathbf{I} + \mathbf{R}^{SU} \cdot (\mathbf{R}^{FU})^{-1} \right) \cdot \mathbf{F} \right\rangle, \tag{3.2c}$$

where $\mathbf{R}^{SU}$ is the resistance tensor that relates the particle stresslet to particle motion relative to the bulk flow, and $\mathbf{R}^{SE}$ relates the stresslet to the bulk rate of strain. To correctly couple microstructure to rheology, $\langle\, \mathbf{S} \,\rangle$ is formulated in terms of $g(\mathbf{r})$ as follows:

$$\langle\, \mathbf{S} \,\rangle = n \int \langle\, \mathbf{S} \,\rangle_2 (\mathbf{r})\, g\,(\mathbf{r})\, d\mathbf{r}, \tag{3.3}$$

where $\langle\, \mathbf{S} \,\rangle_2(\mathbf{r})$ is the average stress on each particle in a pair configuration. This stress is a result of interactions of the individual pair and their interaction with the rest of particles at each pair separation $\mathbf{r}$. $\langle\, \mathbf{S} \,\rangle_2$ is formulated following (3.2) relations, replacing $\langle\,\rangle$ with $\langle\,\rangle_2$. We approximate the conditional pair averages appearing in the formulation of the stress as outlined below.

3.1. *Brownian stress,* $\left\langle \mathbf{S}^{B} \right\rangle$

Following (3.2*a*) and (3.3), Brady (1993) divided the Brownian stress contribution to two parts:

$$n \left\langle \mathbf{S}^{B} \right\rangle = \mathbf{\Sigma}^{B1} + \mathbf{\Sigma}^{B2}. \tag{3.4a}$$

$$\frac{\left\langle \mathbf{\Sigma}^{B1} \right\rangle}{\eta\dot{\gamma}} = -Pe^{-1} \frac{27}{4\pi} \phi^2 \int \mathbf{nn} g ds. \tag{3.4b}$$

$$\frac{\left\langle \mathbf{\Sigma}^{B2} \right\rangle}{\eta\dot{\gamma}} = Pe^{-1} \frac{27}{4\pi} \phi^2 \int \left\langle \mathbf{R}^{SU} \cdot (\mathbf{R}^{FU})^{-1} \right\rangle_2 \cdot \nabla g d\mathbf{r}, \tag{3.4c}$$

where $\mathbf{n}$ is the unit vector along the line of centers, from particle 1 to 2. The advantage of this separation is that $\mathbf{\Sigma}^{B1}$, which is evaluated through a straightforward surface integration, becomes the dominant Brownian contribution for large ϕ (Brady 1993). To

compute the second term, $\left\langle \mathbf{R}^{SU} \cdot (\mathbf{R}^{FU})^{-1} \right\rangle_2$ is needed. Very near contact, pairwise lubrication interactions dominate and $\left\langle \mathbf{R}^{SU} \cdot (\mathbf{R}^{FU})^{-1} \right\rangle_2 \to \left(\mathbf{R}^{SU} \cdot (\mathbf{R}^{FU})^{-1} \right)_{pair}$ as $r \to 2$, where subscript *pair* refers to the isolated pair system; this quantity goes to zero as r^{-2} for $r \gg 2$. The pair distribution function, ∇g, is maximum at contact. Hence the main contribution to the stress comes from the boundary layer volume (Brady & Morris 1997) near contact, and $\mathbf{\Sigma}^{B2}$ is approximated as

$$\frac{\left\langle \mathbf{\Sigma}^{B2} \right\rangle}{\eta \dot{\gamma}} \sim Pe^{-1} \frac{27}{4\pi} \phi^2 \int_{bl} \left(\mathbf{R}^{SU} \cdot (\mathbf{R}^{FU})^{-1} \right)_{pair} \cdot \nabla g d\mathbf{r}, \tag{3.5}$$

where the subscript *bl* refers to integration being carried out inside the boundary layer. We define the boundary layer as the volume adjacent to the contact surface where the angularly averaged pair distribution function is larger than unity: $\tilde{g}(r) \geqslant 1$. This formulation converges to the exact form for dilute suspensions when only pair interactions are considered, and provides a reasonable approximation for concentrated suspensions.

3.2. *Interparticle force stress,* $\left\langle \mathbf{S}^P \right\rangle$

We consider the influence of the hard-sphere force, $\mathbf{F}^{HS}$, and lubrication force, $\mathbf{F}^{lub}$. Recall that $\mathbf{F}^{lub}$ is introduced to mimic hydrodynamic interactions, so the role of this force on the stress will be considered hydrodynamic for the stress calculation. We model $\mathbf{F}^{HS}$ using a steep short-range repulsion negligible at any r except very small distances from the hydrodynamic contact surface. Since $\left\langle \mathbf{R}^{SU} \cdot \mathbf{R}^{FU^{-1}} \right\rangle_2 \to r\hat{\mathbf{r}}\hat{\mathbf{r}}$, the term in parenthesis in (3.2c) goes as $r-2$ for individual pairs near contact. On the other hand, from (2.22), $\mathbf{F}^{HS} \to (r-2)^{-1}$ only at contact. In fact, $\langle \mathbf{S}^P \rangle_2$ is zero except at contact in a true hard-sphere suspension, which makes $\langle \mathbf{S}^P \rangle$ identically zero. Because a steep repulsive force is used to model the hard-sphere interactions, $\langle \mathbf{S}^P \rangle_2$ will be non-zero in a thin layer at the contact surface. This layer becomes thinner as the repulsive force becomes steeper with increase of τ in (2.22). A scaling analysis shows $\left\langle \mathbf{S}^P \right\rangle \sim g(\mathbf{r} = 2\hat{\mathbf{r}})\Delta r$ where

$\Delta r \sim \tau^{-1}$ is the thickness of the layer over which the repulsive force decays to zero which makes $\langle \mathbf{S}^P \rangle \sim O(\tau^{-1})\langle \mathbf{S}^B \rangle$. Therefore the contribution from interparticle forces on the bulk stress is negligible compared to Brownian and hydrodynamic contributions, and will not be further considered here.

3.3. *Hydrodynamic stress,* $\langle \mathbf{S}^H \rangle$

The hydrodynamic stress term requires an approximation of the conditionally averaged hydrodynamic resistances, $\mathbf{R}^{SE}$ and $\mathbf{R}^{SU}$, whose average form is less clear than that of $\mathbf{R}^{FU}$. The singular nature of resistance functions at contact and the need for a renormalization quantity to make the integrals converge adds to the difficulties even in case of an isolated pair (Batchelor & Green 1972*a*). We assume that the stress contribution is maximized near contact due to lubrication interactions, so that the hydrodynamic stress can be approximated by the boundary layer lubrication stresses. The main contribution to the hydrodynamic stress comes from the constraint of relative pair movement along the line of centers (driven by the extensional portion of the bulk flow). We therefore focus on the stress induced by relative motion of the pair along the line of centers ($\hat{\mathbf{r}}\hat{\mathbf{r}}$ component) and ignore the stress generated by pair angular and rotational motion ($\mathbf{I} - \hat{\mathbf{r}}\hat{\mathbf{r}}$ component). For the case of particles nearly touching, the lubrication theory gives $\mathbf{R}^{SE} \sim \mathbf{R}^{FE}\hat{\mathbf{r}}a$ and $\mathbf{R}^{FE} \sim \mathbf{R}^{FU}\hat{\mathbf{r}}a$. Also, from the Lorenz reciprocal theorem $\mathbf{R}^{SU} = (\mathbf{R}^{FE})^T$ (the superscript T here implies transpose). Thus, using (2.9), the average $\hat{\mathbf{r}}\hat{\mathbf{r}}$ component of the stress on each particle near contact can be written

$$\frac{n\langle \mathbf{S}^H \rangle}{\eta\dot{\gamma}} \sim \frac{27}{16\pi}\phi^2 \int_{bl} R^{FU}_{rr} U_r \hat{\mathbf{r}}\hat{\mathbf{r}} g \, d\mathbf{r}, \tag{3.6}$$

where U_r is the relative radial velocity, with $U_r \propto r - 2$ as $r \to 2$. The quantity $R^{FU}_{rr} \sim (2(r-2))^{-1}$ yielding $R^{FU}_{rr} \cdot U_r = O(1)$ at contact. The stress is controlled by the force with which pairs are pushed together (or pulled apart) along their line of centers near contact.

Note that $\hat{\mathbf{r}}\hat{\mathbf{r}}$ in (3.6) and $\mathbf{nn}$ in (3.4*b*) are different presentation of the same quantity; this is done to differentiate volume integrals using $\hat{\mathbf{r}}\hat{\mathbf{r}}$ space from surface integrals using $\mathbf{nn}$. Brady & Bossis (1988) showed in early Stokesian Dynamics (SD) results that the added force due to large concentration surrounding a pair near contact (where resistance is strictly by the intervening fluid) causes pairs to approach more rapidly near contact as the concentration is increased: two particles nearly touching find themselves in an increased 'effective' shear rate. This concept is seen in the boundary layer scaling analysis by Brady & Morris (1997) for hydrodynamic stress in concentrated suspensions, where a modified Péclet number, or dimensionless effective shear rate, used the high frequency dynamic viscosity, $\eta_\infty(\phi)$. Foss & Brady (2000) and Sierou & Brady (2002) showed that this scaling agrees well with SD results for shear stress; however, the scaling was not applicable to particle pressure and normal stress differences. The advantage of our approach is that, rather than scaling the effective shear rate, the radial velocity of a pair comes naturally out of the forces predicted by the theory. This enables us to study in detail how the relative motion and probability distribution impact on the magnitude and trend of particle pressure and normal stress differences.

4. Solution technique

Equation (2.18) is nonlinear due to the product of pair distribution functions resulting from the closure approximation. We solve this equation by using an iterative technique. An initial guess for $g(\mathbf{r})$ is obtained by ignoring the many-body integral terms. We thus first solve the dilute-limit equation for g, with conditional averages equal to the well-known isolated pair hydrodynamic functions. The resulting convection-diffusion equation is solved numerically by a finite element technique to obtain $g_{dilute}(\mathbf{r})$, which in turn is used to evaluate the integrals of the conditional averages appearing in (2.21) and (2.25).

The calculated average values then replace the isolated pair values in (2.16), and the modified differential equation is solved to obtain $g(\mathbf{r})$. The process is repeated until the iterations yield a converged $g(\mathbf{r})$. The convergence criterion used here is $\frac{g^i_{max} - g^{i-1}_{max}}{g^i_{max}} < 10^{-3}$ where g^i_{max} is the maximum value of g at i^{th} iteration.

The mesh generation for FEM was carried out by discretizing the $\mathbf{r}$ space in spherical coordinates, $\mathbf{r} = (r, \theta, \varphi)$. The pair microstructure satisfies the symmetry $g(\mathbf{r}) = g(-\mathbf{r})$. Also, for simple-shear flow we must have $g(r, \theta, \varphi) = g(r, \theta, -\varphi)$. These symmetry properties reduce the calculation to a quarter of the full domain, i.e. $2 \leqslant r < \infty$, $0 \leqslant \theta \leqslant \pi$ and $0 \leqslant \varphi \leqslant \frac{\pi}{2}$. Equally spaced nodes were used in the θ and φ directions, with$\Delta\ \theta = \pi/24$ and$\Delta\ \varphi = \pi/24$. For accurate calculation of $g(\mathbf{r})$ at $Pe \gg 1$, several radial nodes should be inside the boundary layer, as seen also in sampling of microstructure (Morris & Katyal 2002). Hence, a structured mesh was generated in the radial direction with node spacing increasing from$\Delta\ r_0$ at the contact surface as follows:$\Delta\ r_j = \Delta r_0 q^{j-1}$ where j is the number of the element and $q > 1$ controls the increase of radial spacing between elements. Here$\Delta\ r_0 = 0.001$ and $q = 1.1$ were chosen for all ϕ and Pe. The outer radius of the computational domain was chosen as $r = 10$, which is found to be sufficiently large to capture all long range correlations for the conditions studied. The influence of mesh density was tested and the results were independent of the mesh density. For instance with$\Delta\ r_0 = 0.0002$,$\Delta\ \theta = \pi/48$, and$\Delta\ \varphi = \pi/48$ the results were within 0.05 relative error of the regular meshing. Integrals involved in calculating conditional average quantities were carried out numerically by discretizing the integration domain for each pair separation $\mathbf{r}$ in the same fashion as described for the FEM calculation.

5. Results

Results are provided separately for the microstructure and rheology. First, the predictions of microstructure are given. We begin by describing results from the perturbation formulation for $Pe \ll 1$ at a range of ϕ. This is followed by a description of the predicted pair distribution function, $g(\mathbf{r})$, for a range of Pe at $\phi = 0.30$ and 0.40, with comparison to the results from Accelerated Stokesian Dynamics simulation at the same conditions. To investigate the variation with concentration at conditions far from equilibrium, predictions of $g(\mathbf{r})$ at $Pe = 10$ over a range of ϕ are also provided and compared with simulations. We note that the bulk of results presented are for $g(\mathbf{r})$ in the shear plane where the effect of external flow on microstructure is maximized, but all calculations are fully three-dimensional. The rheological predictions based on the computed microstructure follow, again with comparison against the findings from simulation.

5.1. *Microstructure*

We begin by considering the form of $g(\mathbf{r})$ computed by regular perturbation expansion at $Pe \ll 1$. Brady & Vicic (1995) showed that for $Pe \ll 1$, the solution to $g^{(1)}(\mathbf{r})$ and $g^{(2)}(\mathbf{r})$ are of the form

$$g^{(1)}(\mathbf{r}) = f(r)(\hat{\mathbf{r}} \cdot \hat{\mathbf{E}} \cdot \hat{\mathbf{r}}), \tag{5.1a}$$

$$g^{(2)}(\mathbf{r}) = -h_2(r)(\hat{\mathbf{r}} \cdot \hat{\mathbf{E}} \cdot \hat{\mathbf{r}})^2 - h_3(r)(\hat{\mathbf{r}} \cdot \hat{\mathbf{E}} \cdot \hat{\mathbf{\Omega}} \cdot \hat{\mathbf{r}}) - h_4(r)(\hat{\mathbf{r}} \cdot \hat{\mathbf{E}} \cdot \hat{\mathbf{E}} \cdot \hat{\mathbf{r}}) - h_5(r)(\hat{\mathbf{E}} : \hat{\mathbf{E}}), \tag{5.1b}$$

where $\hat{\mathbf{E}}$ and $\hat{\mathbf{\Omega}}$ are the rate-of-strain and rate-of-rotation tensors, made dimensionless by the shear rate, $\dot{\gamma}$, of the imposed shear flow. In earlier work, Wagner & Ackerson (1992) showed that (5.1*a* –5.1*b*) can be presented in terms of a finite number of spherical harmonics:

$$g^{(1)}(\mathbf{r}) = g_{2,-2}(r)Y_{2,-2} \tag{5.2a}$$

$$g^{(2)}(\mathbf{r}) = g_{00}(r)Y_{00} + g_{20}(r)Y_{20} + g_{22}(r)Y_{22} + g_{40}(r)Y_{40} + g_{44}(r)Y_{44}. \tag{5.2b}$$

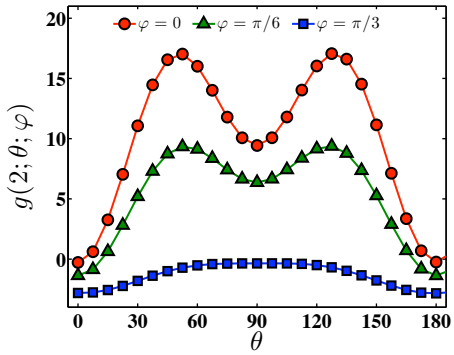

FIGURE 2. The angular variations of the perturbation solution $g^{(2)}(\mathbf{r})$ at the contact surface and azimuthal angles $\varphi = 0,\ \pi/6,\ \pi/3$ for $\phi = 0.40$ suspension.

Solutions to $g^{(1)}$ and $g^{(2)}$ were obtained here by three-dimensional FEM calculations, with no presumed functionality for the solution; however, the computed $g^{(1)}$ and $g^{(2)}$ were decomposable to (5.2*a* – 5.2*b*) with very good accuracy. Figure 2 shows $g^{(2)}(\mathbf{r})$ as a function of θ at $r = 2$ and different φ for a suspension of volume fraction $\phi = 0.40$. The results are given for $0 \leqslant \theta \leqslant \pi$ since $g(r,\theta,\varphi) = g(r,\pi + \theta,\varphi)$. The variation is similar for other concentrations, but the magnitude of the $g^{(2)}$ is a strong function of ϕ. This is evident from figure 3 which presents the values of the harmonic coefficients at contact as a function of ϕ when the solutions are decomposed onto (5.2*a*) and (5.2*b*). The data at $\phi = 0$ is the predictions of the dilute theory of Brady & Vicic (1995). The results are given for $\phi \leqslant 0.50$; no convergent solution could be obtained for $g^{(1)}(\mathbf{r})$ at higher ϕ.

Here and hereafter, structural results are from the full theory, as opposed to the perturbation results above. Figure 5.1 shows the pair distribution function at contact in the shear plane (x - y) at $Pe = 0.10$, 0.20 and 1 for $\phi = 0.30$ and 0.40. The simulation results for $Pe = 0.10$ and 0.20 are noisy, and as a result only the simulations at $Pe = 1$ are presented for comparison. The angular variations of $g(2;\theta)$ for both concentrations have a sinusoidal form at $Pe = 0.10$, as expected for $Pe \ll 1$. For $\phi = 0.30$ the angular variation remains similar as Pe is increased. By contrast, the changes in angular variation

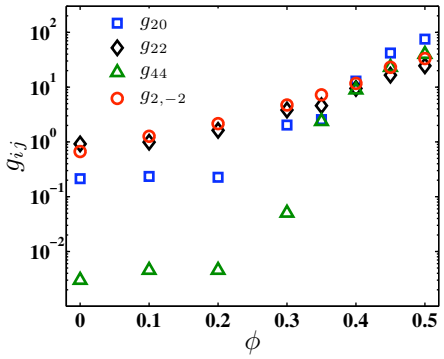

FIGURE 3. The values of spherical harmonic coefficients at $r = 2$ obtained by decomposing the perturbation solutions based on the the forms given by (5.2a – 5.2b).

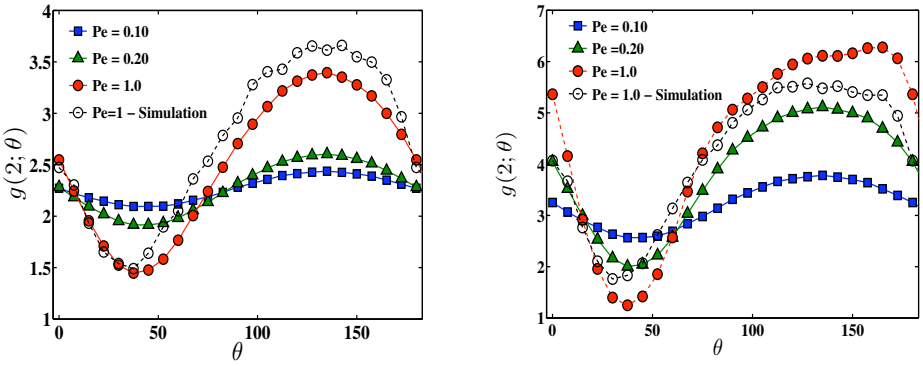

(a) (b)

FIGURE 4. Pair distribution function at contact in the shear plane from the solution of the full pair equation for $Pe = 0.10,\ 0.20$, and 1: (a) $\phi = 0.30$ and (b) $\phi = 0.40$.

are significant for $\phi = 0.40$; for example, consider the appearance of a secondary peak in $g(2;\theta)$ for $Pe = 1$ in both simulation and theory.

Figure 5.1 compares the predicted $g(\mathbf{r})$ for $\phi = 0.40$ and $Pe = 1$ with simulation results restricted to the shear plane. The results are given for half of the plane, recalling that $g(\mathbf{r}) = g(-\mathbf{r})$. The half circle in the center is the excluded volume region, $r < 2$. The theory captures the near contact anisotropy and the main features of the pair microstructure away from contact, including the next nearest neighbor peak in the compressional quad-

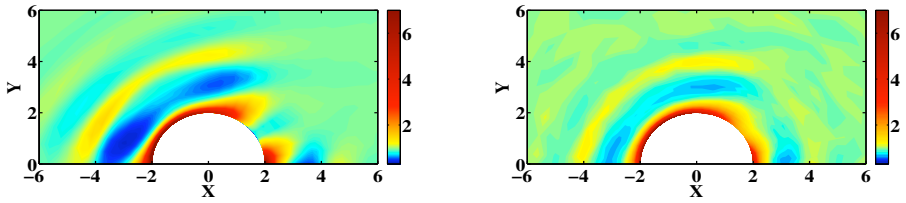

(a) Theory (b) Simulation

FIGURE 5. The pair distribution function, g, in the shear plane for $Pe = 1$ and $\phi = 0.40$ suspensions: (a) Theory prediction (b) results of simulation samplings. The colorbar is the same for the two figures.

rant (near $r = 4$) and the zones depleted of pair correlation. A discrepancy is seen as the distortion of pair microstructure is predicted to be stronger than observed in simulation.

The pair distribution function at contact, $g(2)$ for brevity, is presented in figure 6 for $Pe = 10$ and different volume fractions, again restricting attention to the shear plane. For $\phi = 0.20$, $g(2)$ shows a maximum in the compressional quadrant for both simulation and theory, while at higher ϕ a secondary peak appears in both cases. The largest value of g moves to angles closer to the flow direction with increase of ϕ, and at $\phi = 0.55$ the maximum is in the flow direction for both simulation and theory. The single peak which is present at lower ϕ remains but becomes lesser in magnitude with increase in ϕ; this peak appears at $\beta \approx 100^o$ for $\phi = 0.30$ and moves to $\beta \approx 120^o$ for $\phi = 0.55$, while for the theoretical prediction the angle is largely unchanged at $\beta \approx 120^o$. We see that an increase of volume fraction not only increases the magnitude of $g(\mathbf{r})$ near contact but also changes the form of the microstructure anisotropy; this is important for its rheological consequences, as it renders simple scaling analysis invalid, in particular for the nonlinear rheology found in the normal stress response of the material. The theory captures the much of the observed anisotropy correctly, but there are systematic deviations from

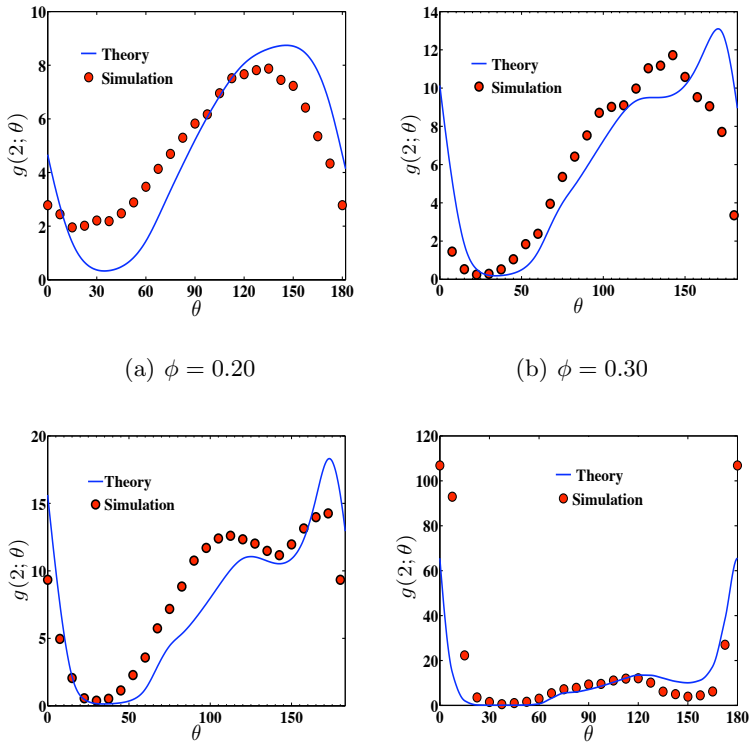

(a) $\phi = 0.20$ (b) $\phi = 0.30$

(c) $\phi = 0.40$ (d) $\phi = 0.55$

FIGURE 6. The pair distribution function at contact in the shear plane for $Pe = 10$: (a) $\phi = 0.20$, (b) $\phi = 0.30$, (c) $\phi = 0.40$, and (d) $\phi = 0.55$.

simulation results. For example, theory over-predicts the value of the pair distribution function along the flow direction for all volume fractions. Also, the peaks in $g(2;\theta)$ appear at larger angles (measured from the flow direction) with respect to simulations. It is interesting to note that the agreement with simulation of the theoretical prediction improves with increasing ϕ, suggesting the approximations made in formulating the theory become more accurate for more concentrated suspensions.

Figure 7 compares $g(\mathbf{r})$ from simulation with theoretical predictions at $Pe = 50$ for $\phi = 0.40$, showing values in the shear plane. The maximum value of g is truncated to 10 to facilitate visualization and comparison of specific features of microstructure (colorbars are identical). At this elevated Pe, a clear boundary-layer structure is seen as found in

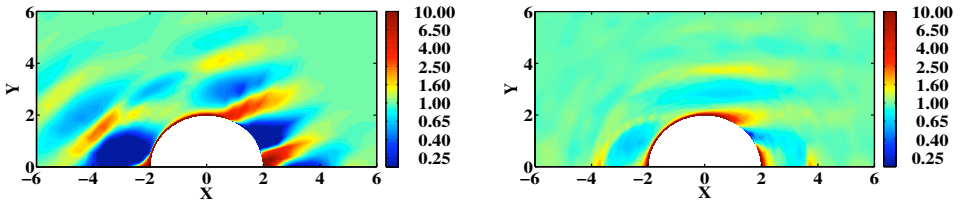

(a) Theory (b) Simulation

FIGURE 7. The pair distribution function at contact in the shear plane for $Pe = 50$ and $\phi = 0.40$: (a) theoretical prediction and (b) results of simulational sampling. The colorbar is the same for both figures.

theory (Brady & Morris 1997) and simulation (Morris & Katyal 2002) studies. In the simulation results presented here, the boundary layer dissipates in a considerably shorter distance from the pair contact surface than seen in the predicted results. In the theoretically predicted structure, the high probability region extends downstream to $r \approx 4$ in the extensional quadrant. The spatial distribution of high and low probability regions is similar for theory and simulation, but the variations are intensified in the theory predictions. The high probability zone convected down stream is a point of clear discrepancy: for simulation, this region continues in the flow direction, while in the predictions it separates from the boundary at an angle with respect to the flow direction.

Figure 8 shows $g(\mathbf{r})$ at contact in the shear plane, for $\phi = 0.40$ with $Pe = 25$ and 50. From figures 8 and 6(c), we see that the main features of the angular variations at contact do not change significantly as Pe increases from 10 to 50; for example, the angles at which the peaks in g are observed remain similar for both simulation and the theory developed here. Increase of shear rate (i.e., Pe) simply amplifies the observed features. The same behavior is observed for other concentrations studied.

The variation of $g(\mathbf{r})$ with the angle φ about the flow axis, with $\varphi = 0$ on the shear plane, is similar for all Pe and ϕ studied. Figure 9 presents contact values of g as a

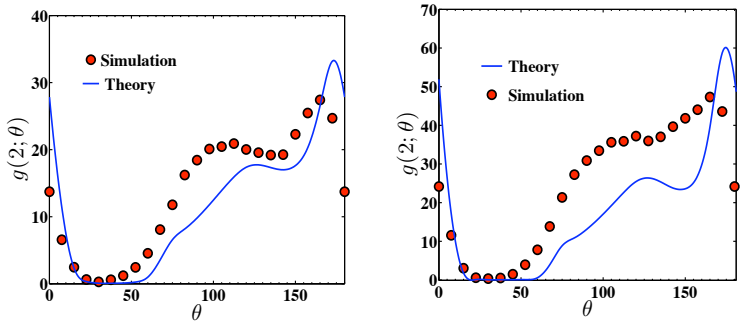

(a) Pe = 25 (b) Pe = 50

FIGURE 8. Angular variations of pair distribution function at contact in the shear plane for $\phi = 0.40$: (a) $Pe = 25$ and (b) $Pe = 50$.

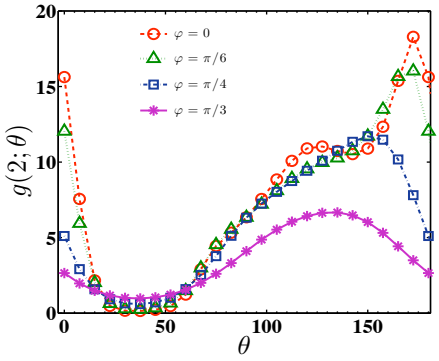

FIGURE 9. Pair distribution function at contact on different planes characterized by the angle φ measured from the shear plane, for $\phi = 0.40$ and $Pe = 10$.

function of θ for different φ at $Pe = 10$ and volume fraction $\phi = 0.40$. Microstructural distortion decreases with increase of the angle φ.

Finally, we present in figure 10 the critical n, with n defined by (2.27), as a function of Pe for $\phi = 0.20$, 0.30, and 0.40. We notice that values of critical n for obtaining a convergent solution decrease as Pe increases, appearing to approach a plateau for each volume fraction. Recall that according to (2.27), larger n results in faster decay of relative radial shear-induced diffusion from its farfield value as the position of interest nears contact (the radial diffusivity is zero at contact). Figure 10 also shows that the values

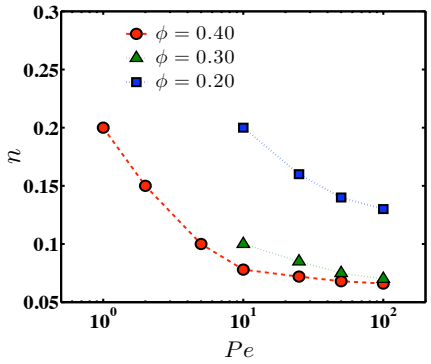

FIGURE 10. The critical n in the shear-induced relative diffusion model (2.27), determined as a function of Pe for $\phi = 0.20$, 0.30, and 0.40.

increase with ϕ, e.g. shear-induced diffusion starts to decay to zero at a larger separation for lower volume fractions. This is consistent with the physical phenomenon modeled, noting that when $r < 4$ and no particle can be placed between, pair relative velocity fluctuations are induced through the particles surrounding the pair. As the suspension becomes more dilute, the behavior is dominated by the pair interactions alone, as these externally-induced fluctuations are weaker and the decay toward the zero value at contact begins at larger separation.

5.2. *Rheology*

We present the predicted steady-shear rheology of suspensions in simple-shear flows. The rheology is characterized by the shear viscosity, $\hat{\eta} = \dfrac{\Sigma_{xy}}{\eta\dot{\gamma}}$, and the first and second normal stress differences, ($\hat{N}_1 = \dfrac{\Sigma_{xx} - \Sigma yy}{\eta\dot{\gamma}}$ and $\hat{N}_2 = \dfrac{\Sigma_{yy} - \Sigma zz}{\eta\dot{\gamma}}$), respectively, with all in dimensionless form. As discussed in §3, the stress associated with the solid phase is divided into hydrodynamic and Brownian stress contributions, with negligible interparticle force contribution, and thus we write

$$\hat{\eta}^T = 1 + \hat{\eta}^B + \hat{\eta}^H, \quad \hat{N}_1^T = \hat{N}_1^B + \hat{N}_1^H, \quad \text{and} \quad \hat{N}_2^T = \hat{N}_2^B + \hat{N}_2^H,$$

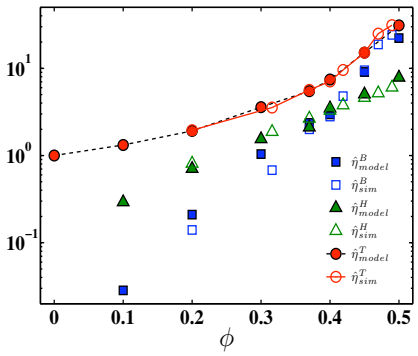

FIGURE 11. Brownian (■, □) and hydrodynamic (▲, △) contributions and total value (○, ●) of zero-shear rate viscosity as a function of volume fraction. Filled symbols present theoretical predictions based on the perturbation solution at $Pe \ll 1$, and the open symbols are the Stokesian Dynamics simulation results of Foss & Brady (2000) at $Pe = 0$.

where superscripts T, B, and H correspond to the total, hydrodynamic, and Brownian stress, respectively. The pair distribution function computed theoretically is used to deduce the Brownian contribution to the particle stress through the relations (3.4*b*) and (3.5); the hydrodynamic contribution is calculated as shown by (3.6).

Figure 11 shows the hydrodynamic and Brownian contributions for the zero-shear rate viscosity based on the perturbation solution for $g^{(1)}(\mathbf{r})$ alongside the Stokesian Dynamics simulation results of Foss & Brady (2000) (these are computed for $Pe = 0$, using a Green-Kubo formulation) as a function of volume fraction. We see excellent agreement between the simulation results and predictions, indicating that the theory predicts the structure accurately near equilibrium. The results are presented for $\phi \leqslant 0.50$, the largest ϕ for which a convergent solution for $g^{(1)}(\mathbf{r})$ can be obtained.

While the zero-shear viscosity is well-understood for hard-sphere dispersions, examination of normal stress differences near equilibrium has been limited (Brady & Vicic 1995). The magnitude of normal stress differences becomes very small near equilibrium, and this makes their experimental measurement difficult. Simulations by Stokesian Dynam-

ics (in standard and accelerated versions) for $Pe \ll 1$ find the fluctuations comparable to the average value as shown by Foss & Brady (2000) and also in the simulations of the current work. This makes comparison with theoretical findings difficult. Considering the functionality of the perturbed microstructure, (5.1*a* - 5.1*b*), and the stress formulations (3.4*b*, 3.5, and 3.6), one can show that $g^{eq}(r)$ and $g^{(1)}(\mathbf{r})$ have no contribution to $\hat{N}_1$ and $\hat{N}_2$. Therefore, the normal stress differences scale as Pe^2 for $Pe \to 0$, and $\chi_1 = \dfrac{\hat{N}_1}{Pe}$ and $\chi_2 = \dfrac{\hat{N}_2}{Pe}$ should be constants in this limit. In figure 12 we present χ_1 and χ_2 as a function of volume fraction. The data for $\phi = 0$ is the dilute theory prediction by Brady & Vicic (1995). Zero-shear viscosity values are given for comparison of the volume fraction dependencies. We see that χ_1 and χ_2 are stronger functions of ϕ than the zero-shear viscosity. This is in agreement with the scaling analysis made by Brady & Vicic (1995), where they proposed $\hat{\eta} \sim (1 - \phi/\phi_m)^{-2}$ and $\chi_i \sim (1 - \phi/\phi_m)^{-3}$ as $\phi \to \phi_m$, a form also used in constitutive modeling by Frank *et al.* (2003). Note also that the magnitudes of $\hat{N}_1$ and $\hat{N}_2$ are similar up to $\phi = 0.37$, above which ϕ the value of $\hat{N}_2$ grows more rapidly than $\hat{N}_1$.

We now consider the rheology determined from the structure deduced based on the full theory. We focus on strongly perturbed microstructures over a range of Pe and ϕ and compare the predicted rheology with simulation results.

Figures 13(a) and 13(b) compare the theoretically predicted values for Brownian and hydrodynamic contributions to shear viscosity to the simulation results for $\phi = 0.30$ and 0.40, respectively, considering a range of Pe. The error bars are the standard deviation of the shear viscosity from its average value, as determined by simulation. The relative magnitude of the error bar with respect to the average value for each Pe is similar for both $\phi = 0.30$ and 0.40, and the error bars are only presented for a few data points at $\phi = 0.40$ to aid visualization. However, we note that the error bars become smaller as Pe

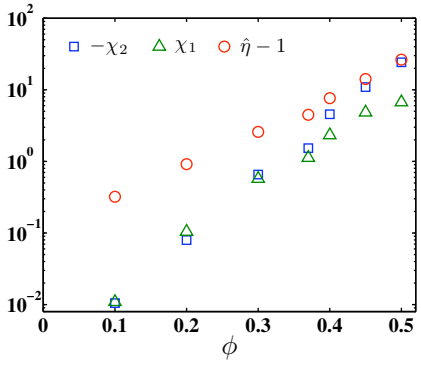

FIGURE 12. Near-equilibrium predictions based on the perturbation analysis of the microstructure, for $\chi_1 = \hat{N}_1/Pe$ and $-\chi_2 = -\hat{N}_2/Pe$ at different volume fractions. The zero-shear viscosity values are also presented.

increases. For both ϕ, the decrease in Brownian viscosity with increasing Pe in the lower range of Pe and increase of hydrodynamic viscosity at high Pe are more pronounced in the predicted results than seen in simulation. This results in stronger shear thinning and shear thickening of the total viscosity for the theory than is observed in simulation. In essence, the theory over-predicts the apparent shear rate, and we find that the agreement is improved if the theoretically predicted results are shifted to higher values of Pe.

Figures 14(a) and 14(b) compare the predicted Pe-dependence of the first and second normal stress differences with simulation results for $\phi = 0.40$. The dotted lines for $0.01 \leqslant Pe \leqslant 0.2$ are the near-equilibrium perturbation results for $\hat{N}_1 = \chi_1 Pe$ and $\hat{N}_2 = \chi_2 Pe$ (see figure 12). The Brownian contributions are given in the inset figures. Unlike simulations which have yet to successfully recover zero normal stress differences very near equilibrium (note the error-bars at $Pe \ll 1$ in figure 14) the predicted normal stress differences tend linearly to zero for $Pe \ll 1$. As a result, a maximum is predicted in $\hat{N}_1$, which changes sign from positive to negative at intermediate Pe. The comparison shows that the signs and general trends for the normal stress difference are predicted correctly. Quantitative agreement is not obtained. Similar to the shear viscosity, the magnitude of

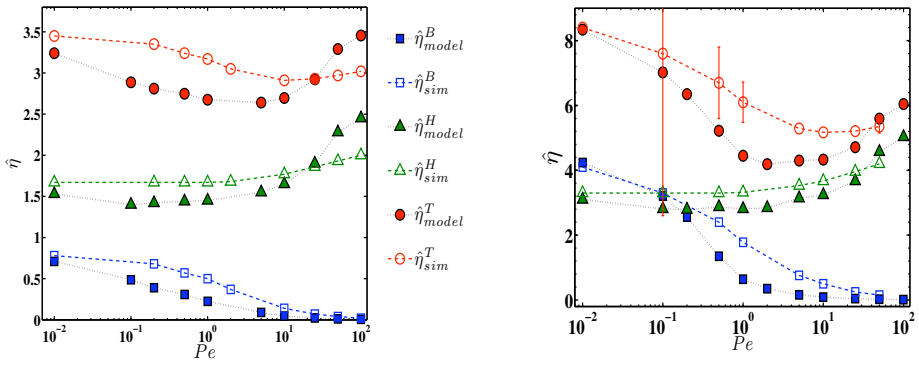

(a) $\phi = 0.30$ (b) $\phi = 0.40$

FIGURE 13. Brownian (■, □) and hydrodynamic (▲, △) contributions and total value (○, ●) of relative viscosity as a function of Pe for (a) $\phi = 0.30$ and (b) $\phi = 0.40$. Filled symbols present the predictions and the open symbols are the results of ASD simulation. The predictions at $Pe = 0.01$ are from the perturbation solutions for the microstructure.

Brownian contribution decreases with Pe more rapidly in predictions than is found in simulation. The absolute value of $\hat{N}_1$ for $Pe \gg 1$ is also significantly over-predicted.

Figure 15 presents the variations of shear viscosity and normal stress differences with volume fraction at $Pe = 10$. Error bars for the simulation data are of the same order of magnitude for $\hat{N}_1$ and $\hat{N}_2$, and are presented only for $\hat{N}_2$. Error bars for shear viscosity are the size of the symbols and are not presented. The results are presented for $\phi < 0.50$ where the system is in the disordered state for all Pe; we avoid consideration of the ordered phase formed at $Pe \geqslant 10$ and $\phi \geqslant 0.50$ in simulations (Kulkarni & Morris 2009). The predictions and simulation results for shear viscosity are in good agreement while for normal stresses, the predictions have the correct sign and are within the range of error-bars. However, the magnitude of first and second normal stress differences are over- and under-predicted, respectively (except at the lowest volume fraction, $\phi = 0.20$). The same trend is observed for higher Pe. This suggests that the anisotropy of the predicted

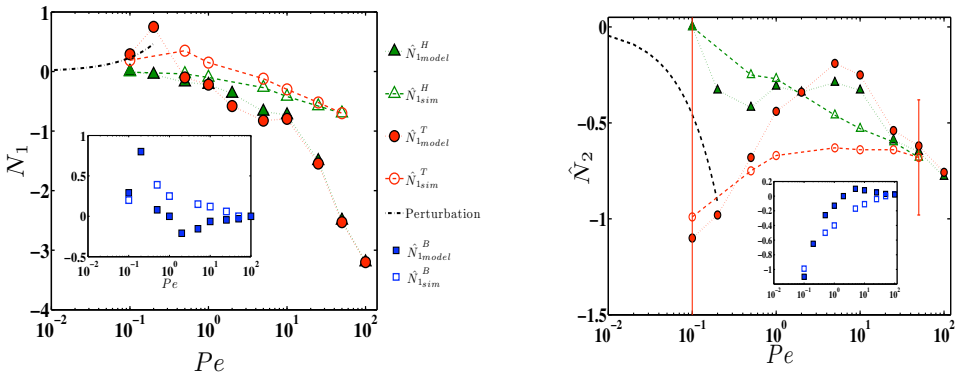

(a) (b)

FIGURE 14. Dimensionless first and second normal stress differences for $\phi = 0.40$ as a function of Pe. The inset figures present the Brownian contributions and the dotted lines at $Pe < 0.20$ are the perturbation results. Filled symbols present the predictions and the open symbols are the results of ASD simulation.

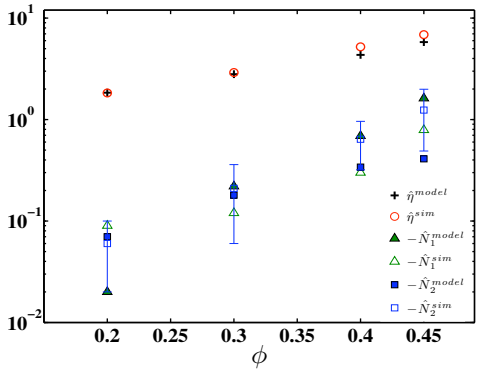

FIGURE 15. The predictions and simulation results of normalized shear viscosity and normal stress differences at $Pe = 10$ and different ϕ.

structure has a systematic deviation from the observed structure in simulation, but the precise basis has not been determined.

5.3. *Discrepancies between theory and simulation*

The theory developed here breaks significant new ground in describing the microstructure of concentrated nonequilibrium dispersions. In order to facilitate further progress in the-

oretical rheology of dispersions using this theory, its shortcomings as seen in comparisons against Stokesian Dynamics simulations are outlined briefly.

As shown in figure 5.1 and 5, the distortion of microstructure from the equilibrium distribution is stronger in theoretical predictions. Direct consequences on the rheology are seen in the stronger predicted shear thinning and shear thickening; in addition, this leads to the decrease in Brownian normal stress differences at lower Pe than seen in simulation, as shown in figure 13 and the insets of figures 14(a) and 14(b). Although the average value of pair distribution function near contact is accurately predicted, the predicted microstructural anisotropies are generally systematically over-predicted: the predictions generally correspond to simulation results seen for either higher ϕ at the same Pe, or at a higher Pe for the same ϕ. This is clearly seen in figure 6 where the locations of the peaks and the value of $g(2;\theta)$ along the flow direction at each ϕ resemble simulation data for a denser suspension at the same Pe. Hence, as shown in figures 6 and 8, the theory over-predicts the peak in $g(2)$ in the flow direction. This impacts upon the rheology as expected: $\hat{\Sigma}_{xx}$ has a stronger compressional (negative) component than the simulations while $\hat{\Sigma}_{yy}$ is less compressive which causes larger negative $\hat{N}_1$ and smaller negative $\hat{N}_2$, as seen in figures 14 and 15.

6. Concluding Remarks

A microstructural theory for concentrated colloidal dispersions of near-hard spheres has been developed based on the Smoluchowski equation. The theory results in an integro-differential equation for the pair distribution function, which for steady simple-shear flow is studied here for Péclet numbers ranging from near equilibrium to strongly sheared conditions. The resulting structure is applied to predict the steady shear rheology of the suspension, and both structure and rheology are compared against our own simulations by

the Accelerated Stokesian Dynamics algorithm. Agreement between simulation and the predictions of the theory are qualitatively very good, with some systematic quantitative discrepancies which have been described.

In formulation of both the microstructural theory and the rheology, approximations based on the central role played by near-contact interactions are employed. These approximations allow a reduction of the many-body hydrodynamic interactions to pair-wise lubrication interactions. The success of these approximations reveals an important aspect of how correlation is transferred in suspensions under shear flow. This theory is motivated in part by the integral equation techniques for equilibrium structure in liquids (Hansen & McDonald 1986). The similarity lies in the coupling of the interaction between the pair of interest to the influence of the bath through probabilistic methods. However, the earlier integral equation techniques are formulated as equilibrium methods and thus their extension to nonequilibrium conditions is unclear. By contrast, the Smoluchowski equation is intrinsically a transport equation for the probability distribution for configurations, and it thus introduces rate dependence naturally. When reduced to a description of the pair distribution function as we have done here, the coupling to the other particles is directly seen in the average forces these particles apply to drive the pair together or apart. This is physically appealing and leads naturally to well-justified, though probably improvable, approximations.

A feature in the theory which is novel is the introduction of a shear-induced component to the relative diffusion of a pair of particles. This diffusivity is closely related to the shear-induced self-diffusivity (Morris & Brady 1996; Sierou & Brady 2004), but in prior treatments of the structure of sheared suspensions has not been implemented. For theories considering dilute dispersions (Brady & Morris 1997), this is justified, but at ϕ not near zero there is clearly a dispersion around the mean pair relative velocity. From a Fokker-

Planck perspective on the microstructure, this dispersion — which will be dominated by shear effects at elevated Pe for moderately to highly concentrated dispersions — must be included to obtain a proper description. In fact, we find that neglecting this dispersion while including the mean forces (due to the surrounding particles) driving a pair interaction leads to divergence in the pair correlation at contact. Hence, we see that the source of the large microstructural correlation seen in the pair distribution function self-consistently contains fluctuations which allow sufficient relaxation to achieve a steady microstructure. The shear-induced relative diffusion in the radial direction contains the only truly tuned fitting parameter in the theory, and this illustrates its centrality to the description of the microscopic dynamics. The shear-induced diffusivity has been simply modeled here, owing to lack of concrete information. Simulational evaluation of the pair relative diffusivity for varying Pe and ϕ appears to be a valuable avenue of study.

The rheological predictions of the theory are qualitatively in agreement with all major observations from simulation and experiment, or predictions of theory where applicable. We predict shear thinning and thickening. The normal stress differences determined are in agreement with theoretical expectations (Brady & Vicic 1995) for $Pe \ll 1$, with this theory extended in the present work. At elevated Pe, the predicted structure deviates from the simulationally determined structure, but predicts the tendency for particles to align along the flow direction for $\phi \geqslant 0.35$, as noted previously by Morris & Katyal (2002). The predictions of the rheology thus deviate from the simulation results. We find that the theory agrees progressively better with simulation results of structure, and hence of rheology, as ϕ increases. This suggests that the approximations based on the dominance of near-contact lubrication interactions are sound but must be modified to obtain quantitative agreement at lower ϕ. We have not in this work sought to make such modifications. Although developed for simple-shear flow, the method is applicable

to general linear-flow kinematics, i.e. for bulk flows which can be written $\mathbf{U}^\infty = \mathbf{G}\cdot\mathbf{x}$ where $\mathbf{G}$ is a constant velocity gradient tensor; for other kinematics than simple shear, abundant simulation results are unfortunately not generally available. A final point to note is that increasing solid fraction at fixed Pe is found to cause an increase in the pair distribution function variations, with the contact values especially amplified. This effect may in part be captured in scaling arguments which seek to rescale the 'driving force' — this amounts to a rescaling of the effective shear rate or Pe. However, the structure is found to differ in a more complex fashion than this with change in ϕ in a sheared dispersion. The anisotropy at contact develops additional features, with development of additional peaks (local maxima) for larger ϕ, and as noted there is a shift to a maximum in pair correlation along the streamlines seen in both the theory developed here and in simulations. This makes a simple scaling of the volume-fraction dependence of the rheology of dispersions suspect.

Acknowledgment

This work was supported by the NSF PREM (DMR-0934206) "Dynamics of Heterogeneous and Particulate Materials," a collaborative program between the City College of New York and the University of Chicago MRSEC.

REFERENCES

Banchio, A. J. & Brady, J. F. 2003 Accelerated Stokesian Dynamics: Brownian motion. *Journal of Chemical Physics* **118** (22), 10323–10332.

Barnes, H. A. 1989 Shearthickening (''dilatancy") in suspensions of nonaggregating solid particles dispersed in Newtonian liquids. *Journal of Rheology* **33** (2), 329–366.

Batchelor, G. K. 1977 The effect of Brownian motion on the bulk stress in a suspension of spherical particles. *Journal of Fluid Mechanics* **83** (01), 97–117.

Batchelor, G. K. & Green, J. T. 1972*a* The determination of the bulk stress in a suspension of spherical particles to order c^2. *Journal of Fluid Mechanics* **56** (03), 401–427.

Batchelor, G. K. & Green, J. T. 1972*b* The hydrodynamic interaction of two small freely-moving spheres in a linear flow field. *Journal of Fluid Mechanics* **56** (02), 375–400.

Bergenholtz, J., Brady, J. F. & Vicic, M. 2002 The non-Newtonian rheology of dilute colloidal suspensions. *Journal of Fluid Mechanics* **456**, 239–275.

Brady, J. F. 1993 The rheological behavior of concentrated colloidal dispersions. *Journal of Chemical Physics* **99** (1), 567–581.

Brady, J. F. & Bossis, G. 1988 Stokesian Dynamics. *Annual Review of Fluid Mechanics* **20**, 111–157.

Brady, J. F. & Morris, J. F. 1997 Microstructure of strongly sheared suspensions and its impact on rheology and diffusion. *Journal of Fluid Mechanics* **348**, 103–139.

Brady, J. F. & Vicic, M. 1995 Normal stresses in colloidal dispersions. *Journal of Rheology* **39** (3), 545–566.

Chen, L. B., Zukoski, C. F. & Ackerson, B. J. 1994 Rheological consequences of microstructural transitions in colloidal crystals. *Journal of Rheology* **38** (2), 193–216.

Foss, D. R. & Brady, J. F. 2000 Structure, diffusion and rheology of Brownian suspensions by Stokesian Dynamics simulation. *Journal of Fluid Mechanics* **407**, 167–200.

Frank, M., Anderson, D., Weeks, E. A. & Morris, J. F. 2003 Particle migration in pressure-driven flow of a Brownian suspension. *Journal of Fluid Mechanics* **493**, 363–378.

Fuchs, M. & Cates, M. E. 2002 Theory of nonlinear rheology and yielding of dense colloidal suspensions. *Physical Review Letters* **89** (24), 248304–248307.

Gao, C., Kulkarni, S. D., Morris, J. F. & Gilchrist, J. F. 2010 Direct investigation of anisotropic suspension structure in pressure-driven flow. *Physical Review E* **81** (4), 041403–041407.

Hansen, J. & McDonald, R. 1986 *Theory of simple liquids*, 3rd edn. Elsevier.

Kim, S. & Karrila, S. 2005 *Microhydrodynamics: Principles and Selected Applications*, 1st edn. 31 East 2nd Street, Mineola, N.Y. 11501: Dover.

Kulkarni, S. D. & Morris, J. F. 2009 Ordering transition and structural evolution under shear in Brownian suspensions. *Journal of Rheology* **53** (2), 417.

Leighton, D. T. & Acrivos, A. 1987*a* Measurement of shear-induced self-diffusion in concentrated suspensions of spheres. *Journal of Fluid Mechanics* **177**, 109–131.

Leighton, D. T. & Acrivos, A. 1987*b* The shear-induced migration of particles in concentrated suspensions. *Journal of Fluid Mechanics* **181**, 415–439.

Lionberger, R. & Russel, W. B. 1997 A Smoluchowski theory with simple approximations for hydrodynamic interactions in concentrated dispersions. *Journal of Rheology* **41** (2).

Mazoor, P. & Van Saarloos, W. 1982 Many-sphere hydrodynamic interactions and mobilities in a suspension. *Physica A: Statistical and Theoretical Physics* **115** (1-2), 21–57.

Morris, J. F. & Boulay, F. 1999 Curvilinear flows of noncolloidal suspensions: The role of normal stresses. *Journal of Rheology* **43** (5), 1213–1237.

Morris, J. F. & Brady, J. F. 1996 Self-diffusion in sheared suspensions. *Journal of Fluid Mechanics* **312**, 223–252.

Morris, J. F. & Katyal, B. 2002 Microstructure from simulated Brownian suspension flows at large shear rate. *Physics of Fluids* **14** (6), 1920.

Rice, A. S. & Lekner, J. 1965 On the equation of state of the rigidsphere fluid. *Journal of Chemical Physics* **42** (10), 3559–3565.

Russel, W. B., Saville, D. A. & Schowalter, W. R. 1995 *Colloidal Dispersions*. 40 West 20th Street, New York, NY 10011-4211, USA: Cambridge University Press.

Sierou, A. & Brady, J. F. 2001 Accelerated Stokesian Dynamics simulations. *Journal of Fluid Mechanics* **448**, 115–146.

Sierou, A. & Brady, J. F. 2002 Rheology and microstructure in concentrated noncolloidal suspensions. *Journal of Rheology* **46** (5), 1031–1056.

Sierou, A. & Brady, J. F. 2004 Shear-induced self-diffusion in non-colloidal suspensions. *Journal of Fluid Mechanics* **506**, 285–314.

Szamel, G. 2001 Nonequilibrium structure and rheology of concentrated colloidal suspensions: Linear response. *Journal of Chemical Physics* **114** (19).

Throop, G. & Bearman, R. 1965 Numerical solutions of the Percus-Yevick equation for the hard-sphere potential. *Journal of Chemical Physics* **42** (7), 2408–2411.

Vermant, J. & Solomon, M. J. 2005 Flow-induced structure in colloidal suspensions. *Journal of physics: Condensed Matter* **17** (4), R187–R216.

Wagner, N. & Ackerson, B. 1992 Analysis of nonequilibrium structures of shearing colloidal suspensions. *Journal of Chemical Physics* **97** (2), 1473–1484.

van der Werff, J. C. & de Kruiff, C. G. 1989 Hard-sphere colloidal dispersions: the scaling of rheological properties with particle size, volume fraction, and shear rate. *Journal of Rheology* **33** (3), 421–454.

Yurkovetsky, Y. & Morris, J. F. 2006 Triplet correlation in sheared suspensions of Brownian particles. *Journal of Chemical Physics* **124** (20), 204908–204919.

Zarraga, I. E., Hill, D. A. & Leighton, D. T. 2000 The characterization of the total stress of concentrated suspensions of noncolloidal spheres in Newtonian fluids. *Journal of Rheology* **44** (2), 185–220.